machines

MDPI

Article

A Verifiable Steady-State Frequency–Velocity Mapping for Desktop FDM Printers Based on an Electromechanical Coupling Framework

Xinfeng Zou [1], Haiyan Miao [1], Baoshan Huang [2,*], Zhen Li [1] and Fengshou Gu [1]

[1] Efficiency and Performance Engineering, University of Huddersfield, Huddersfield HD1 3DH, UK; xinfeng.zou@hud.ac.uk (X.Z.); h.miao@hud.ac.uk (H.M.); f.gu@hud.ac.uk (F.G.)
[2] Institute of Intelligent Manufacturing Technology, Guangdong Mechanical & Electrical Polytechnic, Guangzhou 510550, China
* Correspondence: jetson_sbs@163.com

Abstract

To monitor online the operational condition and quality of a desktop fused deposition modeling (FDM) printer, the dynamics of vibro-acoustics must be accurately understood. In this paper, an electromechanical coupling (EMT) framework is established to relate the dynamics of stepper actuation, the transmission chain, and machine motion, deriving a steady-state frequency–velocity mapping for steady or near steady printing segments. The mapping is evaluated by numerical calculation to obtain a theoretical drive frequency for different toolpath directions and commanded printing velocities. Validation is performed on the experiment platform I. Drive-side vibration is measured by an accelerometer mounted on the *x*-axis beam near the motor end. An acoustic channel is recorded as an auxiliary qualitative cross-check rather than for quantitative error evaluation. For steady printing segments, the dominant frequency in drive-side vibration is compared with the theoretical drive frequency. In the tested steady segments and toolpath directions, the relative error remained below 3%. In a further case study, the G-code is modified to introduce two constant printing velocity segments (40 mm/s and 80 mm/s) within the same continuous record, enabling a direct comparison of dominant frequencies between two steady segments. The results show that, under open-loop stepper drive and within the steady/near steady scope adopted here, a drive-related dominant frequency can be observed stably in the *x*-axis beam vibration response and matches the theoretical drive frequency. When the commanded constant printing velocity is doubled, the dominant frequency in drive-side vibration in the corresponding steady segment changes by approximately a proportional factor. This study provides a verifiable drive referenced frequency–velocity mapping for steady segments under the tested configuration and a traceable frequency reference for steady segment comparisons within the same print record in subsequent case studies.

Keywords: fused deposition modeling (FDM); theoretical drive frequency; electromechanical coupling (EMT); steady-state frequency–velocity mapping; drive-side vibration

Check for updates

Academic Editor: Nicola Ivan Giannoccaro

Received: 17 March 2026
Revised: 27 April 2026
Accepted: 29 April 2026
Published: 2 May 2026

Copyright: © 2026 by the authors. Licensee MDPI, Basel, Switzerland. This article is an open access article distributed under the terms and conditions of the Creative Commons Attribution (CC BY) license.

1. Introduction

Fused deposition modeling (FDM) is extensively utilized in engineering because of its low cost and broad applicability [1,2]. Print quality and process stability remain sensitive to machine condition and process consistency [1]. Recent broader assessments of additive manufacturing have also highlighted the continued development of material extrusion

technologies together with increasing attention to sustainability, material selection, and application-oriented process optimization [3,4]. As a result, studies on the FDM process, monitoring, and defect identification have expanded [5,6]. Commonly used monitoring signals include vibration, acoustics, vision, and electrical signals, which have been used to characterize anomalies, failures, and process-related defects during fabrication [2,6]. For desktop FDM systems, a key practical question is how to use measurable signals to track the printing process with sufficient reliability [2,5].

For material extrusion processes (FDM/FFF), existing studies have systematically reviewed monitoring objectives, sensor technologies, signal processing procedures, and representative diagnostic strategies, while distinguishing monitoring tasks related to process state, geometric deviation, layer deposition, and surface quality [1,5–8]. Recent application-oriented studies have further shown that vibration, acoustics, vision, thermal imaging, electrical signals, force, and flow-related measurements can each provide different but useful forms of process information in desktop and laboratory-scale FDM/FFF systems [2,9–23]. Recent broader assessments of additive manufacturing have also highlighted the continuing development of material-extrusion-based technologies in relation to materials, applications, and process optimization [3,4]. What remains less clearly resolved in desktop FDM monitoring is how a physically traceable drive-related reference can be linked to printing velocity and verified through a structural measurement on the drive side. In specific applications, data-driven in situ monitoring has been used for anomaly recognition and state identification [1,5,9]. Acoustic emission and acoustic observations have been used to identify filament breakage and related process anomalies [16,17] and have also been extended to broader fault diagnosis and to tracking deformation and warpage trends [18,19]. Vision-based and digital-twin-based methods have been used to evaluate geometric deviations [20], while thermal imaging, machine-learning-based monitoring, and multi-view vision methods have been used for quality inference, mechanical property prediction, online correction, and real-time structural validation or decision making [10,11,21–23]. Electrical, force, and flow-related signals have also been used to monitor extrusion conditions, polymer flow states, and warpage-related interactions [2,12,13]. In addition, current-based monitoring and multi-sensor information fusion have been used for state identification and anomaly detection [9,14,15].

Vibration and acoustic signals are commonly used to observe FDM process states [1,6,17,24]. In desktop FDM applications, different sensing routes provide different types of information and involve different practical limitations. Vision-based methods are effective for geometric deviation evaluation, surface inspection, and online correction tasks [7,10,20]. Their applicability in desktop FDM, however, still depends on stable image acquisition conditions during printing. Acoustic measurements are simple to deploy and non-contact, but they are sensitive to environmental noise and background vibration [8,24]. Electrical, force-, and flow-related measurements can reveal local process conditions such as extrusion state, interaction, and flow behavior [2,12,13]. By contrast, vibration measured near the drive-side is more directly linked to the stepper actuation, transmission chain, and supporting structure, and sensor location affects the observability of dominant components [24–27]. These two sensing channels are attractive for desktop FDM monitoring because they can be implemented with comparatively simple instrumentation and have already been used in practical condition monitoring studies [17,24]. Previous studies have shown that spectral features in vibration or acoustic signals can reflect differences in process conditions and support state discrimination or anomaly-related assessment [17,28]. Compared with extruder-end vibration or global acoustics, drive-side vibration is measured closer to the motor-side excitation source and is therefore more suitable, in the context of this study, for tracking drive-related

dominant components. During FDM motion, the measured response is influenced by both the executed toolpath and the behavior of the stepper drive system [29–31]. To reduce the influence of transient changes, the analysis in this study focuses on steady printing segments. Stepper drives are widely used in small precision positioning systems, including 3D printers [30,31]. For a fixed configuration, the theoretical drive frequency implied by controller step pulses is deterministic and repeatable and can therefore serve as a reference for checking process consistency. Meanwhile, open-loop stepper operation, micro-stepping control and motor-side torque variations can introduce drive-related content into vibration and acoustic responses [30–33]. In vibration-based monitoring, dominant frequencies can be extracted from structural measurements, and sensor placement influences their observability [24]. Base or external vibration can also affect the measured response and is considered in the analysis [25]. More broadly, condition monitoring studies have also noted that acoustic measurements are sensitive to environmental noise and background vibrations [8]. With this context, the question addressed here is whether the theoretical drive frequency can be stably observed in drive-side vibration during steady printing segments and linked to printing velocity in a verifiable manner. Although existing FDM monitoring studies have used vibration and acoustic signals for anomaly recognition, state classification, and quality-related inference, they rarely establish an explicit steady segment correspondence between theoretical drive frequency, printing velocity, and the dominant component observed in drive side vibration for desktop FDM printers operating under open-loop stepper drive. The present work addresses this missing link by establishing an electromechanical coupling (EMT) framework, deriving the corresponding frequency–velocity relation, and validating it by steady segment checks and a constant-velocity doubling case.

Although existing FDM monitoring studies cover a range of sensing and diagnostic approaches, for desktop FDM printers operating under open-loop stepper drive, the relation between the theoretical drive frequency and printing velocity is often not stated in an explicit form, and direct validation of the steady segment correspondence using drive-side vibration remains limited. Compared with anomaly recognition, state classification, or quality inference, validation of the chain linking the theoretical drive frequency, printing velocity, and the dominant frequency in drive-side vibration is still insufficient. To support online monitoring of operational condition and quality in desktop FDM printers, this study establishes an electromechanical coupling (EMT) modeling framework and derives the mapping between theoretical drive frequency and printing velocity under open-loop stepper drive, which is validated by within-segment checks and a constant velocity doubling case. Under the tested conditions, the dominant frequency identified from drive-side vibration agrees with the theoretical drive-frequency reference with a relative error below 3%, and a commanded constant velocity change from 40 mm/s to 80 mm/s produces an approximately proportional shift in the dominant frequency between the two steady segments. Experiments are conducted on the experimental platform I (EP-I platform). Drive-side vibration is measured by an accelerometer mounted on the x-axis beam, while acoustic signals are used only for supplementary qualitative comparison. The quantitative analysis is limited to steady or near-steady printing segments; nonstationary acceleration/deceleration transitions are excluded, and printhead module end displacement is not evaluated in this work. The paper is organized as follows. Section 2 establishes an electromechanical coupling (EMT) modeling framework and derives the frequency–velocity mapping under steady conditions. Section 3 uses MATLAB-based numerical calculation to obtain the theoretical drive frequency for different toolpath directions and commanded printing velocities and then performs validation in steady printing segments on the EP-I platform, with the acoustic channel used only as a supplementary qualitative observation.

Section 4 modifies the G-code to introduce a constant printing velocity doubling case within the same continuous record and compares the changes in the dominant frequency in drive-side vibration between two steady printing segments to assess the applicability of the proposed mapping under this condition.

2. EMT Model and Steady-State Formulation

Figure 1 outlines the main workflow of this study. The work starts with the development of a general EMT model and the derivation of the steady-state frequency–velocity mapping. Experimental validation is then conducted under different printing paths, followed by an additional verification under the velocity-doubling case. Chapter 2 presents the EMT model and the steady-state mapping, which provide the basis for the subsequent analysis.

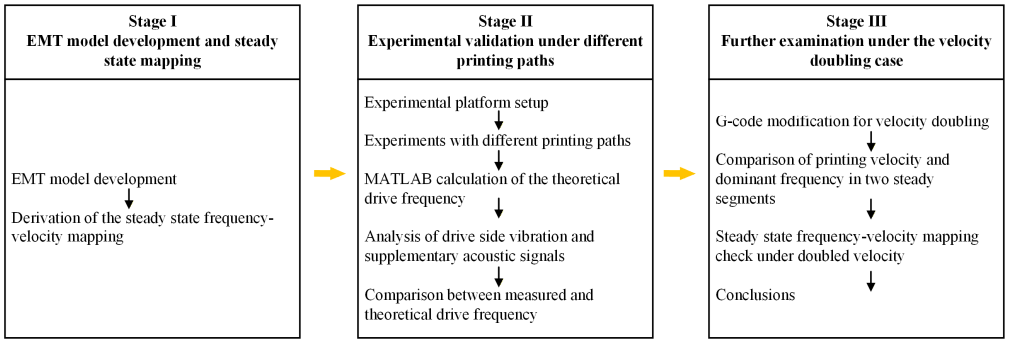

Figure 1. Overall workflow of the present study.

2.1. Motion System Description

During fused deposition modeling (FDM), the position and motion trajectory of the printhead module are determined by the printer motion system, which directly governs whether material can be deposited along the prescribed printing path. In desktop FDM systems, the in-plane motion associated with each layer is typically realized by a stepper motor combined with a synchronous belt transmission. Figure 2 illustrates the basic x-axis arrangement of the printhead module motion system. The motor drives the synchronous belt through the pulley set, and the resulting belt motion produces linear displacement of the printhead module relative to the build platform. For clarity in the following sections, the motor shaft, timing pulley, idler pulley, and printhead module are denoted as subsystems M_1 to M_4, respectively. As shown in Figure 2, M_1 is the drive unit formed by the stepper motor; M_2 and M_3 are the transmission units formed by the timing pulley and idler pulley, respectively; and M_4 is the printing unit formed by the printhead module. This arrangement shows that the printing motion originates from the drive unit and is transmitted to the printhead module through the transmission chain. During printing, motion commands are progressively realized through the mechanical transmission structure and are finally converted into printhead module motion, under which material is continuously deposited and shaped [26,27]. This subsection first outlines the system configuration, which serves as the basis for the modeling and analysis presented later.

Existing modeling studies on FDM systems are mainly distributed across several different parts of the process. Modeling of filament feeding and melting extrusion has mainly been used to describe the relationship among nozzle clogging, backpressure, and extruder motor current, thereby supporting nozzle condition monitoring [2]. Dynamic analysis of synchronous belt transmission systems has mainly focused on responses such as belt tension fluctuation, pulley angular vibration, and transmission error [26]. Nonlinear dynamic modeling of Cartesian FFF gantries has incorporated belt compliance and structural vibration to analyze motion errors and support predictive control design [27]. For

two-phase hybrid stepper motors, simplified mathematical and Simulink models based on the direct-quadrature (d-q) transformation have also been reported to describe the relationships among voltage, current, torque, and angular motion [34]. More specific studies are also available for the drive side of desktop FDM systems. For hybrid stepper motors, microstepping strategy, command waveform shape, torque ripple, and cogging-related effects have all been shown to influence motion response and positioning behavior [30–33]. On the monitoring side, structural vibration has been used to reflect process-state changes, and the observability of dominant components has been shown to depend on sensor location and boundary vibration conditions in desktop FDM platforms [24,25]. Taken together, they do not yet describe the full actuation-to-motion chain of a desktop FDM printer within a single framework. On this basis, the present work introduces the general form of the EMT model, in which the drive unit, transmission unit, and printing unit are organized according to the actual path of energy and motion transfer, thereby providing the basis for the subsequent modeling and analysis. Compared with subsystem-level models, the proposed EMT framework links stepper actuation, synchronous belt transmission, and printhead motion in one coupled description and is used here to derive a traceable relation between the theoretical drive-frequency reference and the drive-side vibration response under steady or near-steady printing conditions.

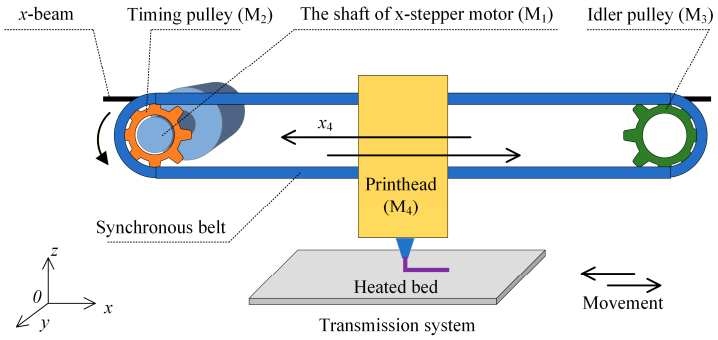

Figure 2. Schematic of the *x*-axis transmission and printhead module motion chain.

2.2. EMT Dynamic Model

In this study, an EMT model is established for the FDM motion system, which covers the stepper motor, the mechanical transmission, and the printhead module. The coupling topology is illustrated in Figure 3. Within this formulation, motor torque, transmission dynamics, and printhead module translation are interpreted in a unified dynamic framework. This model serves as the basis for the subsequent analysis of the coupled motion system.

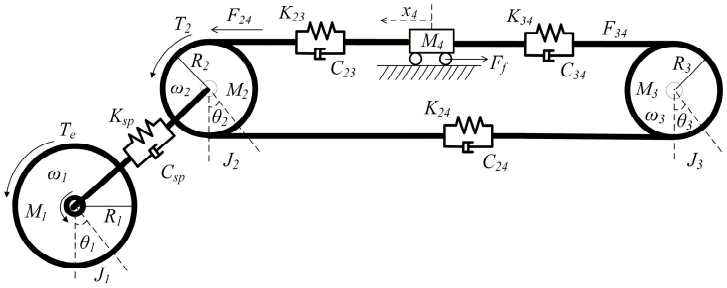

Figure 3. Schematic of the EMT structure and subsystem indices (*x*-axis).

The electrical frequency f_{elec} is defined as the phase-current commutation event rate, while the theoretical drive frequency f_{drive} is defined as the full step equivalent drive frequency (i.e., 1.8° full step event rate). The two frequencies are related by

$$f_{drive} = k \cdot f_{elec} \tag{1}$$

where k is determined by the commutation scheme and the number of motor phases (e.g., $k = 4$ for a two-phase stepper motor under a typical four-step commutation). This relation establishes a shared time reference between the controller output and the motor's electrical state. The electromagnetic torque is determined by the phase currents and rotor position, which is expressed as [34]

$$T_e = k_t \cdot [i_A \cdot sin(N_r \cdot \theta_m) + i_B \cdot cos(N_r \cdot \theta_m)] \tag{2}$$

where k_t is the torque constant, N_r is the number of rotor pole pairs, and θ_m denotes the rotor position. The motor shaft dynamics is determined by the balance among inertia, viscous damping, and external load torque, as summarized in Equation (3).

$$J_1 \cdot \dot{\omega_1} + B_1 \cdot \omega_1 + T_{dm} + T_l = T_e \tag{3}$$

where J_1 the total rotational inertia on the rotor side, B_1 the viscous damping coefficient, T_{dm} the mechanical damping term, and T_l the load torque is transmitted from the transmission. To link step pulses to angular speed, the angle θ_{step} and the full step number per revolution N_{fs} are introduced as follows to relate the theoretical drive frequency f_{drive} to the average angular speed $\omega_1(t)$.

$$\omega_1(t) \approx \theta_{step} f_{drive}(t),\ \theta_{step} = \frac{2\pi}{N_{fs}} \tag{4}$$

By rearranging Equation (3) and then dividing by J_1, the first-order form is obtained by Equation (5).

$$\frac{d}{dt}(\omega_1(t)) = \frac{1}{J_1}[T_e(t) - B_1\omega_1(t) - T_l(t) - T_{dm}(t)] \tag{5}$$

2.2.1. Elastic Coupling: Shaft-Pulley

Elastic coupling between the motor shaft and the timing pulley is represented by an equivalent torsional stiffness k_{sp} and damping c_{sp}, leading to the load torque in

$$T_l = k_{sp}(\theta_1 - \theta_2) + c_{sp}(\omega_1 - \omega_2) \tag{6}$$

where θ_2 and ω_2 are the angular displacement and angular speed of the timing pulley. The torque transmitted back to the motor side is therefore governed by the relative displacement and speed between the shaft and the pulley. The timing pulley angular momentum balance is written as,

$$J_2\dot{\omega_2} + B_2\omega_2 + T_{belt} = T_l \tag{7}$$

where J_2 is the equivalent pulley inertia referred to the timing pulley, B_2 is the viscous damping coefficient, and T_{belt} denotes the resisting torque from the synchronous belt.

2.2.2. Transmission Coupling: Pulley-Belt-Printhead

Synchronous belt elastic deformation is described via the belt extension, defined as

$$z_{belt}(t) = R_{2r}\theta_2(t) - x_4(t),\ \dot{z_{belt}}(t) = R_{2r}\omega_2(t) - \dot{x_4}(t) \tag{8}$$

where $x_4(t)$ is the printhead module displacement along the x-axis and $R_{2r} = R_2 + \Delta r$ is the effective pulley radius. The positive directions of θ_2 and x_4 are chosen consistently with the positive x-direction, so that $z_{belt} > 0$ corresponds to belt tensioning and a positive pulling force on the printhead module. The belt driving force is modeled by combined elastic and damping contributions,

$$F_{24}(t) = k_{belt} \cdot z_{belt}(t) + c_{belt} \cdot \dot{z_{belt}}(t) \tag{9}$$

where k_{belt} and c_{belt} denoting the equivalent belt stiffness and damping, respectively. In this study, $k_{belt} = K_{23}$ and $c_{belt} = C_{23}$ to match the subsystem indexing. The belt stiffness is expressed in a variable form,

$$k_{belt} = \frac{C_{sp} \cdot b}{L(t)} \tag{10}$$

where C_{sp} is the belt material constant, b is the belt width, and $L(t)$ is the belt length. The belt reaction on the pulley is represented as a resisting torque,

$$T_{belt}(t) = F_{24}(t) \cdot R_{2r} \tag{11}$$

From Equations (8)–(11), the synchronous belt behaves as a torsional elastic damping load on the pulley side scaled by R_{2r}, and the resulting reaction torque is transmitted to the timing pulley [26]. The x-axis translational dynamics of the printhead module are given by

$$M_4 \ddot{x_4} + F_{fric}(\dot{x_4}) = F_{24}(t) + d_{4x}(t) \tag{12}$$

where M_4 is the equivalent mass of the printhead module, F_{fric} is the resultant friction force along the x direction, and $d_{4x}(t)$ denotes the equivalent external disturbance. To avoid non-physical discontinuities, friction is described using a continuous expression [35,36],

$$F_{fric}(\dot{x_4}) = \left[F_c + (F_s - F_c) e^{-(|\dot{x_4}|/v_s)^j} \right] sgn(\dot{x_4}) + c_f \dot{x_4} \tag{13}$$

where F_c is the Coulomb friction force, F_s is the peak static friction, v_s is the Stribeck velocity, $j \in [1, 2]$ is the shaping exponent, and c_f is the viscous friction coefficient.

2.2.3. Unified First Order Model

With the formulation above, the motor shaft, timing pulley, and printhead module constitute a closed-loop coupled system. For a compact representation, the state vector is defined as

$$s = [\theta_1, \omega_1, \theta_2, \omega_2, x_4, v_4]^T,\ v_4 = \dot{x_4}$$

The motion system dynamics can then be written in a unified first order form. For the motor shaft, angular position and angular speed satisfy,

$$\dot{\theta_1} = \omega_1,\ \dot{\omega_1} = \frac{1}{J_1}[T_e - B_1\omega_1 - T_l - T_{dm}] \tag{14}$$

For the timing pulley, rotational motion is governed by,

$$\dot{\theta_2} = \omega_2,\ \dot{\omega_2} = \frac{1}{J_2}[T_l - B_2\omega_2 - F_{24}R_{2r}] \tag{15}$$

The printhead module translational motion along the x-axis is described by,

$$\dot{x_4} = v_4,\ \dot{v_4} = \frac{1}{M_4}\left[F_{24} + d_{4x} - F_{fric}(v_4)\right] \tag{16}$$

In these equations, the electromagnetic torque T_e, the load torque T_l, and the belt driving force F_{24} are given by Equations (2), (6), and (9), respectively. The EMT model therefore captures the dynamic coupling among motor actuation, the transmission chain, and printhead module motion, including feedback induced by transmission load. The EMT model retains full dynamic terms for the motion system. Because the printhead module typically travels at near constant velocity over most toolpath segments in practical FDM printing, steady printing assumptions are introduced next to simplify the model and derive a steady-state mapping between printing velocity and the theoretical drive frequency (f_{drive}).

2.3. Steady-State Frequency–Velocity Mapping

During FDM printing, printhead module velocity remains constant in most of the toolpath segments. Under these steady printing conditions, the EMT model introduced in Section 2.2 can be simplified by neglecting fast transient terms, which allows a steady-state mapping between the theoretical drive reference (f_{drive}) and printing velocity to be derived. For steady segments, printhead module motion is well approximated as uniform translation along the toolpath. The average acceleration of the printhead module is very small and is neglected in the analysis, i.e., $\ddot{x}_4 \approx 0$. The synchronous belt is treated as quasi-steady, so that the elongation rate variation remains limited where $\ddot{z_{belt}} \approx 0$. As a result, z_{belt} varies slowly and belt force F_{24} can be treated as approximately constant over a steady segment. Under these conditions, torsional deformation between the motor shaft and timing pulley is small, and the angular speeds can be approximated as $\omega_1 \approx \omega_2$.

These simplifications are intended for steady or near-steady constant-velocity segments, where the commanded motion is maintained over a sufficiently long interval and transient acceleration effects do not dominate the response. In the present study, the subsequent validation is restricted to such segments, rather than to the full printing process including acceleration, deceleration, and frequent path-transition events. According to Equation (4) and the belt elongation definition, the timing pulley angular speed can be expressed as

$$\omega_2 = \frac{\dot{x}_4 + \dot{z_{belt}}}{R_{2r}} \tag{17}$$

It is worth noting that under steady printing, $\omega_1 \approx \omega_2$. For a toolpath with printing velocity v, defined as the commanded (nominal) toolpath velocity, and path angle θ relative to the x-axis, the velocity component in x-direction is $\dot{x}_4 = v cos\theta$. Since variations in belt elongation are negligible ($\dot{z_{belt}} \approx 0$), the above expression reduces to

$$f_{drive} \approx \frac{N_{fs}}{2\pi R_{2r} \eta_{mesh}} v cos\theta \tag{18}$$

where η_{mesh} denotes an equivalent meshing efficiency factor. In summary, Equation (18) has been obtained by reducing the full motion model in Equations (14)–(16) over steady segments. The equation is applicable when the acceleration terms are negligible ($\ddot{x}_4 \approx 0$) and the belt elongation rate variation is limited ($\ddot{z_{belt}} \approx 0$). These conditions yield $\omega_1 \approx \omega_2$ and lead to the kinematic mapping used as the theoretical drive frequency in the subsequent validation. When the printing process departs from the steady or near-steady condition assumed above, the validity of the simplified mapping can be reduced. For example, during acceleration/deceleration or frequent contour transitions, the assumption $\ddot{x}_4 \approx 0$ no longer holds well. Likewise, when belt-tension variation, belt relaxation, or stronger transmission-chain dynamics become more pronounced, the assumptions $\ddot{z}_{belt} \approx 0$, $\dot{z}_{belt} \approx 0$, and approximately constant F_{24} may become less accurate. Under such conditions, the approximation $\omega_1 \approx \omega_2$ may also weaken, and additional transient or transmission-

related components may enter the measured response. As a result, the theoretical drive reference may no longer correspond as clearly to the observed dominant frequency as it does in the steady segments selected in this study. The proposed mapping should therefore be interpreted as a segment level relation for steady or near-steady motion, rather than as a universal description of the entire printing process.

3. Experimental Validation

To validate the steady-state EMT formulation in Section 2, MATLAB R2024b is employed to compute f_{drive} under steady-state conditions by using the steady-state EMT mapping. Steady-state printing experiments have been performed on a commercial desktop FDM platform. Drive-side vibration and the corresponding acoustic response have been recorded. Consistency is evaluated by identifying the dominant frequency in drive-side vibration in steady segments and comparing it with f_{drive}.

3.1. Experimental Setup and Data Acquisition

The steady-state experimental platform (EP-I) is implemented on a Shenzhen Creality 3D Technology Co., Ltd. (Shenzhen, China). CR-6 commercial desktop FDM 3D printer, with a simplified schematic shown in Figure 4. The platform acquires drive-side vibration and acoustic response signals. Drive-side vibration is measured using a YMC PIEZOTRONICS YMC 122A200 (Yangzhou, China) single-axis IEPE accelerometer, with a sensitivity of 200 mV/g and a measurement range of ±25 g pk. Acoustic response is measured using an ICP microphone preamplifier manufactured by Beijing Acoustic Sensing Technology Ltd. (Beijing, China), with a sensitivity of 50 mV/Pa. All channels are synchronously recorded using a YE6231 data acquisition system, sampled at 2.5 kHz during the printing process, and exported in MAT format. Because microphone-based acoustic measurements can drift with ambient conditions and temperature, the acoustic channel is retained only as a supplementary qualitative observation [28,37]. Quantitative analysis is therefore restricted to steady segments, where the dominant frequency in drive-side vibration can be identified more reliably. For the synchronous-belt drive used in the EMT calculation, the timing pulley in the M_2 subsystem is a 20-tooth pulley with an effective radius $R_2 + \Delta r = 6.254$ mm. These transmission parameters are taken from the manufacturer's nominal geometric specifications and are used as platform-specific inputs in the present calculation; they are not obtained through separate experimental calibration in this study.

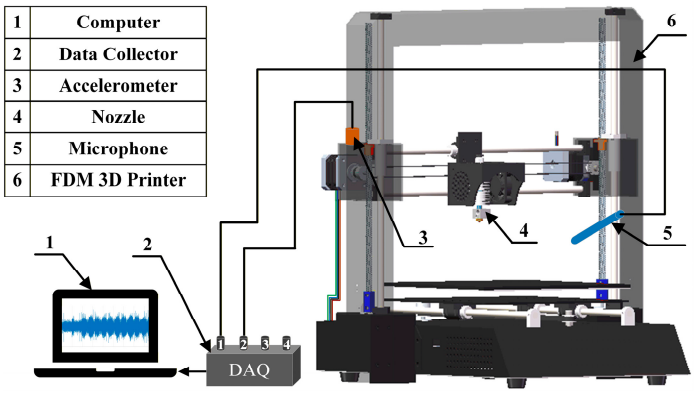

Figure 4. Experimental platform I (EP-I): simplified schematic and installation layout.

The accelerometer was mounted on the x-axis beam near the x stepper motor end to capture drive-side structural vibration, while the microphone recorded the acoustic radiation during the printing process. Data acquisition covered the entire printing process to ensure continuity under steady-state conditions.

A specimen with a 20 × 20 mm cross-section was printed for the experiments. The sliced toolpath, shown in Figure 5, includes perimeter paths and infill paths. The perimeter (represented by the green line) is formed by axis aligned straight runs, while the infill (represented by yellow line) is deposited in a single, prescribed direction. Let θ denote the angle between the perimeter direction and the infill direction; the x-axis velocity component satisfies $v_x = vcos\theta$. In this study, $\theta = 45°$. The theoretical drive frequency for the perimeter is denoted as $f_{P-drive}$, and that for the infill as $f_{I-drive}$. For a path direction angle β (defined as the angle between the x-axis and the perimeter direction), the corresponding theoretical drive frequency is calculated as

$$f_{I-drive} = f_{P-drive} \cdot cos\ \theta \tag{19}$$

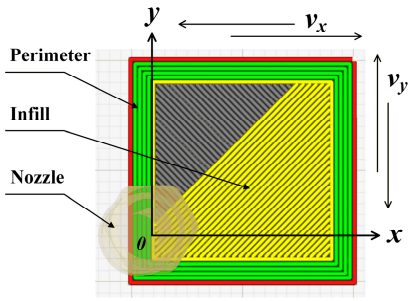

Figure 5. Cross sectional models and printhead module path with infill/perimeter.

As shown in Figure 6, there are four placement angles that have been tested: $\beta = 0°$, 30°, 45°, and 60°, where $\beta = 0°$ indicates that the perimeter is parallel to the x-axis. Printing parameters were kept constant: nozzle temperature 195 °C, printing bed temperature 60 °C, layer height 0.2 mm, PLA material, and G-code velocity was set to 40 mm/s.

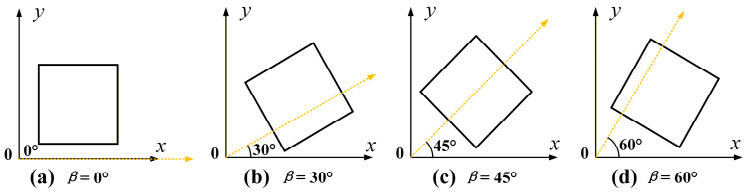

Figure 6. Path placement angles.

3.2. Signal Configuration and Dominant Frequency Extraction

Under open-loop stepper drive and near steady-state operation, the theoretical drive frequency f_{drive} is determined from the G-code defined motion command through the steady-state EMT mapping, which in turn determines the corresponding x-axis velocity component v_x. In this study, f_{drive} is used as the input reference and is computed in MATLAB from the steady-state EMT mapping. The numerical implementation was carried out in MATLAB R2024b. For each selected segment, the theoretical drive frequency was obtained by direct evaluation of the steady-state mapping using the commanded printing velocity and path angle from the corresponding G-code segment. The platform-specific settings and geometric parameters used in the calculation were matched to the EP-I configuration described in Section 3.1. No additional parameter fitting or iterative optimization was used in the MATLAB calculation. The printer settings and geometric parameters used in the calculation are matched to the experimental configuration of the EP-I platform.

As shown in Figure 7, an accelerometer is mounted on the x-axis beam near the stepper motor end to measure drive-side vibration. From the measured drive-side vibration, the drive related dominant frequency in drive-side vibration is identified and denoted as f_{x-beam} (i.e., the dominant frequency extracted from the x-axis beam vibration signal in

steady segments). Comparing f_{x-beam} with f_{drive} across operating conditions provides an experimental assessment of the steady-state manifestation of the EMT mapping. An acoustic signal is recorded simultaneously, but it is used only as an auxiliary observation.

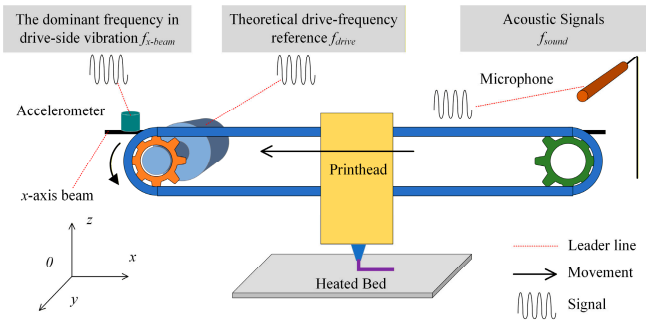

Figure 7. Transmission pathways and correlations among multisource state signals.

The steady-state EMT mapping derived in Section 2 was implemented in MATLAB to calculate the theoretical drive frequency corresponding to different path directions and commanded printing velocities ($f_{P-drive}$ and $f_{I-drive}$). Because the process is still in a transient stage at the beginning of the printing process, especially during nozzle and bed temperature regulation, frequency identification and comparison were performed only on steady segments selected from the middle to late stage of the printing process. In the present study, these steady segments were selected from commanded constant-velocity portions of the G-code, typically from the third layer onward, where the signal was less affected by the start-up stage and nozzle–bed interaction. Within these portions, time intervals with stable vibration response were used for dominant-frequency extraction, and the same selection principle was applied consistently across all compared cases. For the selected steady segments, the vibration signal was first examined in the time domain and then transformed into the frequency domain for peak identification. Time-frequency representation was used only to assist visual inspection of the signal evolution, whereas the quantitative comparison was based on the spectrum of the selected steady segment. The dominant frequency in the drive-side vibration, f_{x-beam}, was defined as the spectral peak with the highest amplitude in the selected steady segment and was compared with the corresponding theoretical drive-frequency reference ($f_{P-drive}$ or $f_{I-drive}$, depending on the segment). The frequency-axis spacing used in the spectrum calculation was $\Delta f = F_s/N$, where F_s is the sampling frequency and N is the number of samples in the selected segment. Because different steady segments had different durations, the corresponding frequency resolution varied from segment to segment, and therefore a single fixed value is not reported for all cases. In the interpretation of the spectrum, harmonics or nearby secondary components were not used as the primary quantitative indicator. Instead, the comparison with the EMT reference was based on the main peak associated with the drive-related response in the selected steady segment.

3.3. Comparison of Theoretical and Experimental Results

Figure 8 summarizes the spectral distributions for four x-angles ($\beta = 0°/30°/45°/60°$). Each row corresponds to one toolpath angle, and each column corresponds to one type of result. Panels (a), (d), (g), and (j) show the MATLAB calculation; panels (b), (e), (h), and (k) show the time–frequency response of the drive-side vibration measured on the x-axis beam; and panels (c), (f), (i) and (l) show the corresponding time–frequency response of the acoustic channel. For $\beta = 0°$, Figure 8a shows the MATLAB calculation based on the steady-state Equation (18): the theoretical drive frequency associated with perimeter printing is approximately 141.5 Hz, with its second harmonic at about 282.5 Hz; the theoretical

drive frequency associated with infill printing is approximately 200 Hz, with its second harmonic at about 400 Hz. The relationship between the two theoretical drive frequency values follows the directional constraint given by Equation (19). Figure 8b shows the time-frequency result of the x-axis beam drive-side vibration, where stable and distinct peaks appear near 140.63 Hz and 199.22 Hz and exhibit a time pattern consistent with the printing sequence. Figure 8c shows the corresponding acoustic time–frequency result. Compared with the vibration channel, the acoustic response shows a different amplitude distribution, and some components are less prominent. However, the main trend remains consistent, with the component near 199.22 Hz still clearly visible. For this reason, the acoustic channel is used only as a qualitative cross-check, whereas the quantitative comparison is based on the drive-side vibration signal.

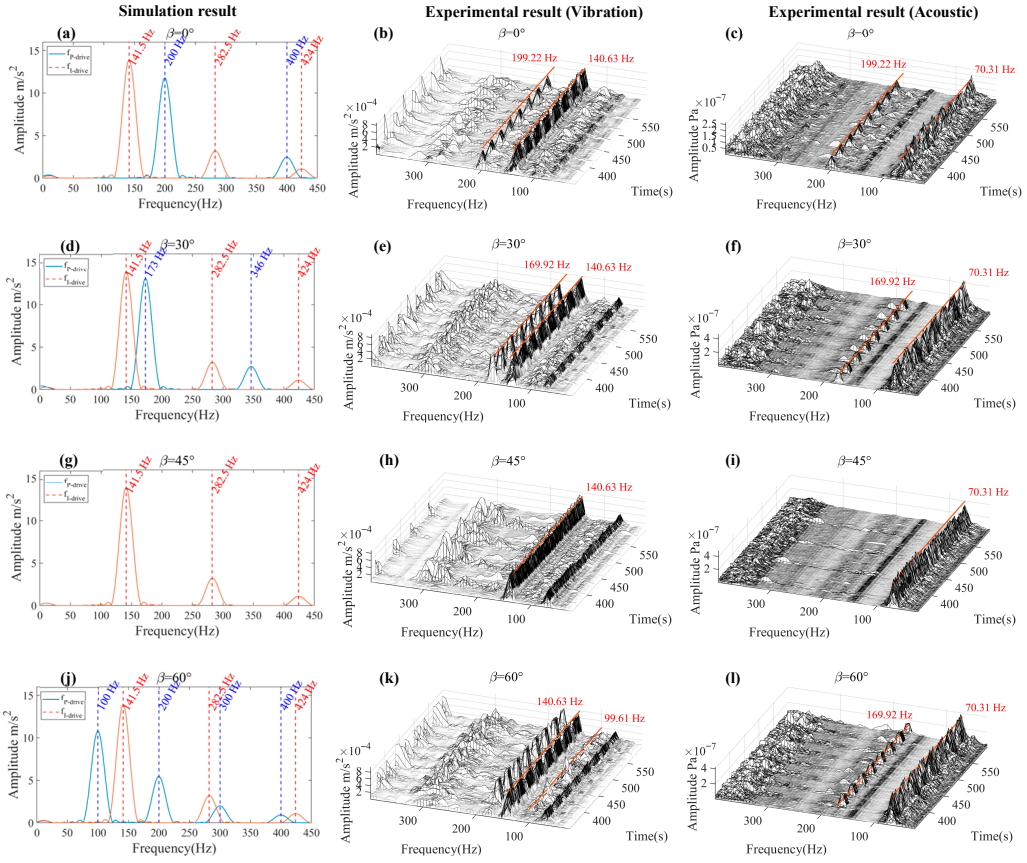

Figure 8. Spectral distributions for four path angles (β = 0°, 30°, 45°, and 60°). Panels (**a**,**d**,**g**,**j**) show MATLAB simulation results; panels (**b**,**e**,**h**,**k**) show the corresponding time–frequency responses of the drive-side vibration; and panels (**c**,**f**,**i**,**l**) show the corresponding acoustic responses. Specifically, (**a**–**c**) correspond to β = 0°, (**d**–**f**) to β = 30°, (**g**–**i**) to β = 45°, and (**j**–**l**) to β = 60°.

For $\beta = 45°$, the two components associated with perimeter and infill printing can be identified simultaneously, and their relationship is consistent with the $cos\theta$ directional term. When $\beta = 30°$ and $\beta = 60°$, the spectral patterns are similar because of the reciprocating motion along the toolpath, while the dominant frequency in the drive-side vibration f_{x-beam} remains consistent with the theoretical drive frequency. The dominant frequencies in drive-side vibration locations are consistent between the two channels. Differences in amplitude distribution and some harmonic components are observed, which do not affect the identification of the drive related components.

Table 1 summarizes the statistical comparison between the theoretical drive frequency calculated in MATLAB and the measured f_{x-beam} (i.e., the dominant frequency in drive-side vibration). The relative error is defined with respect to the theoretical drive frequency.

The values reported in Table 1 correspond to representative steady segment comparisons under the listed operating conditions. A full repeatability analysis was not established for every condition listed in the table. However, additional tests conducted at other commanded printing velocities showed the same mapping trend with small deviations from the theoretical reference. The results therefore indicate that the error remains small under steady-state conditions and provides a baseline for the subsequent analysis.

Table 1. Perimeter/infill frequencies: theoretical–measured comparison and relative error under different toolpaths.

Printing Status	v_x (mm/s)	Simulated $f_{P-drive}$	Experiment f_{x-beam}	Relative Error	Simulated $f_{I-drive}$	Experiment f_{x-beam}	Relative Error
$\beta = 0°$	40	200.64 Hz	199.22 Hz	0.71%	141.87 Hz	140.63 Hz	0.88%
$\beta = 30°$	34.64	173.75 Hz	169.92 Hz	2.25%	141.87 Hz	140.63 Hz	0.88%
$\beta = 45°$	28.28	141.87 Hz	140.63 Hz	0.88%	141.87 Hz	140.63 Hz	0.88%
$\beta = 60°$	20	100.32 Hz	99.61 Hz	0.71%	141.87 Hz	140.63 Hz	0.88%

3.4. Discussion and Summary

Experimental results show that, for steady printing segments, f_{x-beam} for different toolpath directions agrees with f_{drive}, with errors of less than 3%. In summary, under open-loop stepper drive and near steady operation, f_{x-beam} is observable in the x-axis beam vibration. Over the tested path directions and drive conditions, f_{x-beam} extracted from the drive-side vibration signal agrees with f_{drive} predicted by the steady-state EMT mapping.

This result verifies the steady-state drive response correspondence using drive-side observations and provides a steady reference for later comparisons. Because printing velocity commands can change during a printing process, a case study has been carried out by varying printing velocity by comparing the dominant frequencies of two constant velocity steady segments within the same continuous record.

4. Case Study: Printing Velocity Switching

In practical printing, a continuous record from a single printing process may contain steady segments at different commanded constant printing velocities. Building on the steady-state mapping established in Section 3, this section introduces a local modification to the G-code in one experiment to create a two level constant printing velocity switch and compares $f_{x-\mathrm{beam}}$ between the steady segments before and after the switch. The purpose is to check whether the steady-state mapping remains observable under this condition. Two sets of comparative figures are provided: in each set, the left panel shows the result under an unchanged printing velocity command, and the right panel shows the result when the commanded constant printing velocity is doubled during a specified printing action. In the right panel, the time frequency representation includes the steady responses before and after the switch, enabling a direct comparison within the same figure. The acceleration and deceleration transition is not treated quantitatively, and the conclusions are limited to the steady segments.

4.1. G-Code Modification and Segment Selection

All tests were conducted on the EP-I platform; its platform configuration, sensor placement, and data acquisition procedure were the same as in Section 3. The printing path and basic process parameters were kept unchanged. The only modification was made to the G-code. Two printing velocity settings were introduced within the same G-code file in a single printing process. For selected constant velocity segments, the commanded printing velocity was set to twice the original value, while the remaining segments retained

the original constant velocity command. To keep the motion direction consistent and to reduce the complexity of localization and comparison, two edge printing segments parallel to the x-axis were selected, and their commanded constant printing velocity was changed from 40 mm/s to 80 mm/s. The two velocities were selected because both fall within a stable and commonly used operating range of the desktop FDM platform used in this study. In addition, 40 mm/s and 80 mm/s form a clear 1:2 ratio, which provides a direct basis for examining whether the dominant frequency in the selected steady segments remains consistent with the steady-state frequency–velocity mapping when the commanded printing velocity is doubled. Diagonal segments were not used because they involve coordinated $x - y$ stepper motor motion and would add unnecessary complexity; this case study is limited to frequency changes between steady segments.

According to the G-code used in this experiment, the edge printing includes four layers. During edge printing, the x- and y-axis stepper motors participate in an alternating manner. Therefore, for the four-layer edge printing, the x-axis stepper motor and the y-axis stepper motor work eight times independently. After printing, the approximate time intervals corresponding to the two modified locations in the G-code were identified. The vibration record was then examined with a local zoom around these intervals to locate the steady motion segments. For each modification, one steady segment at a commanded constant 40 mm/s is selected as the comparison segment. The same steady segment selection rule as defined in Section 3.2 was used to extract the comparison segments before and after the velocity change. For the present case study, one steady segment at a commanded constant 40 mm/s and one steady segment at a commanded constant 80 mm/s were selected for comparison.

4.2. Dominant Frequency Comparison (Drive-Side Vibration)

The experimentally acquired signals include drive-side vibration, obtained by an accelerometer mounted on the x-axis beam, and a global acoustic record. Figure 9 provides the drive-side vibration results, where each figure corresponds to one of the two printing velocity modifications and contains two panels: (a) a baseline case with an unchanged printing velocity command and (b) a modified case where the commanded constant printing velocity is doubled during a specified printing action. The corresponding acoustic results are summarized in Figure 10. In both channels, the printing velocity switch is identifiable, and the dominant spectral content is concentrated within 10–500 Hz. Across the switch from 40 mm/s to 80 mm/s, the dominant peak shifts from approximately 199.22 Hz to approximately 398.44 Hz, while the component near 199.22 Hz is strongly reduced or becomes indistinguishable. For the x-axis-parallel segments used in this case study, the path direction remains fixed, and Equation (18) therefore implies an approximately proportional relation between the theoretical drive frequency and the commanded printing velocity. The commanded velocity ratio is 80/40 = 2.00, whereas the corresponding dominant-frequency ratio is 398.44/199.22 $\approx$ 2.00. This directly quantifies the observed proportional change under the selected steady segment conditions and supports the frequency–velocity relation implied by Equation (18).

In panel (b), the time–frequency result is taken from the same continuous record, allowing the steady responses before and after the switch to be distinguished within a single plot. Using Figure 9 as an example, the identified f_{x-beam} matches the corresponding theoretical drive frequency f_{drive} reported in Table 2, with a relative error below 3%, and the peak locations are repeatable within the locally zoomed steady windows. The acoustic channel exhibits the same shift trend (Figure 10) and is used only for qualitative cross-checking; conclusions are drawn primarily from the drive-side vibration comparison.

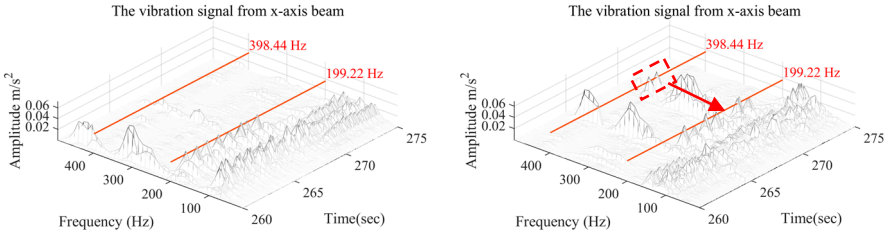

(a) **Trial 1**: 40 mm/s baseline (b) **Trial 1**: velocity changed from 40 mm/s to 80 mm/s

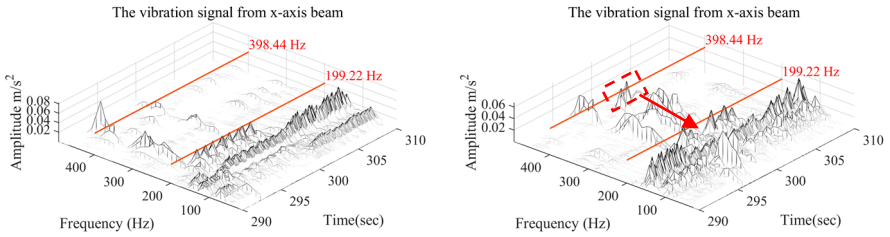

(c) **Trial 2**: 40 mm/s baseline (d) **Trial 2**: velocity changed from 40 mm/s to 80 mm/s

Figure 9. STFT based time-frequency responses of vibration signals from the *x*-axis beam.

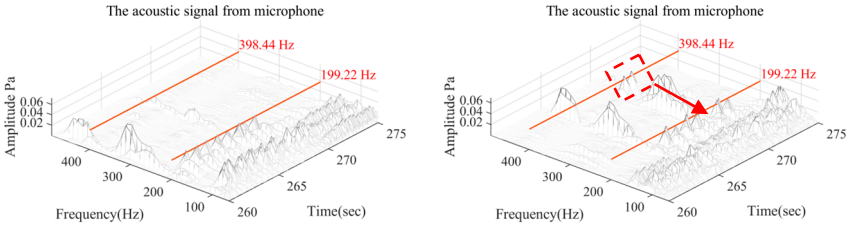

(a) **Trial 1**: 40 mm/s baseline (b) **Trial 1**: velocity changed from 40 mm/s to 80 mm/s

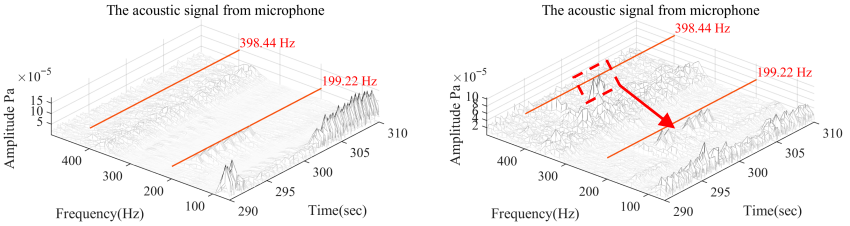

(c) **Trial 2**: 40 mm/s baseline (d) **Trial 2**: velocity changed from 40 mm/s to 80 mm/s

Figure 10. STFT based time-frequency responses of global acoustic signals.

Table 2. Printing perimeter: f_{drive} and f_{x-beam} (two steady-state velocities).

Printing Status	v_x (mm/s)	Theoretical $f_{P-drive}$	Experiment f_{x-beam}	Relative Error
$\beta = 0°$	40	200.64 Hz	199.22 Hz	0.71%
$\beta = 0°$	80	401.28 Hz	398.44 Hz	0.71%

4.3. Applicability Scope

Section 3 shows that for steady printing at a constant commanded velocity, the measured $f_{x-\text{beam}}$ remains consistent with the theoretical drive frequency f_{drive} obtained from the steady-state mapping. In this section, two within-build velocity-doubling modifications are introduced in the same continuous record, producing two independent comparison sets; both show the same $f_{x-\text{beam}}$ shift behavior. Local zoom and $f_{x-\text{beam}}$ extraction from the steady segments indicate that when the commanded constant printing velocity increases from 40 mm/s to 80 mm/s, $f_{x-\text{beam}}$ shifts from approximately 199.22 Hz to approximately

398.44 Hz and remains stable within each steady segment. This observation is consistent with the steady-state mapping validated in Section 3.

Physically, this shift indicates that the dominant drive-related vibration component follows the change in the commanded actuation state, rather than remaining fixed at a structure-only resonance. This is important for monitoring because it shows that the drive-side vibration signal contains a traceable frequency feature that can be used to distinguish steady operating conditions and to check the consistency of the theoretical drive-frequency reference under controlled printing segments. Figures 9 and 10 also show that the spectral response does not change from one stable peak to the other in an instantaneous steady manner at the velocity-transition interval. Around the velocity change instant, the spectral feature becomes temporarily less concentrated than in the two steady segments, and a short transition can be observed before the new dominant peak becomes stable. Although this transition interval is not analyzed quantitatively in the present study, it qualitatively shows that the drive-related frequency component is less clearly defined during the velocity-change interval than in the steady segments. This supports restricting the quantitative frequency comparison to steady or near-steady motion.

It is worth noting that the conclusions are limited to comparisons between steady segments at two commanded constant printing velocities within the same continuous record. Because the acceleration/deceleration interval is brief and non-stationary, it is excluded from quantitative analysis. The proposed mapping should therefore be interpreted as a segment-level relation for steady or near-steady motion, rather than as a universal description of the entire printing process.

5. Conclusions and Future Work

This study establishes an electromechanical coupling (EMT) framework for a desktop FDM printer and derives the mapping between theoretical drive frequency and printing velocity in steady or near-steady segments under open-loop stepper control. The mapping is evaluated by numerical calculation and validated through within-segment checks and segment-to-segment comparisons, including a constant velocity doubling case. Experiments were conducted, and drive-side vibration was measured using an accelerometer mounted on the x-axis beam, while acoustic signals were used only for supplementary qualitative comparison.

- EMT steady-state mapping referenced to the theoretical drive frequency (f_{drive}). A steady-state EMT mapping framework is formulated, where load torque links the electrical side and the mechanical transmission side. An explicit relation is obtained between the theoretical drive frequency and the commanded printing velocity for steady (or near steady) constant velocity segments under open-loop stepper drive.
- Validation of theoretical calculations against observations in steady segments. The steady-state relation is evaluated in MATLAB to obtain the theoretical drive frequency. The theoretical drive frequency is compared with the dominant frequency in the drive-side vibration ($f_{x-\mathrm{beam}}$) extracted from drive-side vibration measurements. The mapping is verified for different toolpath directions in steady segments. The acoustic channel is retained only as a supplementary qualitative check, while quantitative evaluation is based on drive-side vibration. For the tested steady segments and toolpath directions, the relative error remains below 3%. Compared with many existing FDM monitoring studies, which often emphasize signal sensitivity qualitatively, the present work provides an explicit and verifiable steady segment frequency–velocity correspondence for a desktop open-loop stepper-driven FDM system.
- Applicability illustrated by a constant printing velocity doubling case. Two steady, constant velocity segments within the same continuous record are compared. The

dominant frequency in drive-side vibration changes with the twofold change in the commanded constant printing velocity, supporting a traceable frequency–velocity correspondence implied by the steady-state EMT mapping. When the commanded constant printing velocity is doubled from 40 mm/s to 80 mm/s, the dominant frequency in drive-side vibration shifts from approximately 199.22 Hz to approximately 398.44 Hz in the corresponding steady segments. For the fixed path direction used in this case study, this result gives a direct quantitative indication that the observed dominant-frequency change follows the twofold velocity increase. Under the tested drive mode and transmission configuration, the mapping is expected to apply to other constant velocity segments within the tested velocity range, provided that the open-loop stepper drive is maintained and steady segments can be identified reliably.

This work focuses on steady-state and near-steady conditions. Nonlinear factors such as friction variation, synchronous belt viscoelasticity, and backlash are simplified and not considered. These effects can reduce the accuracy of the simplified mapping when they become sufficiently pronounced, because they may alter the transmission response assumed to remain quasi-steady over the selected segment. Some parameters are sensitive to platform configuration and operating conditions and may require experimental identification and calibration prior to deployment. Validation is conducted on a commercial desktop FDM printer using PLA and regular toolpaths. The tested constant velocity range is 40–80 mm/s under the configuration considered. Acceleration and deceleration transitions are non-stationary and are excluded from quantitative analysis. More specifically, friction variation, belt-tension variation, belt relaxation, and stronger transmission-chain dynamics may weaken the assumptions used in the EMT reduction, while non-steady motion can make the observed dominant frequency less clearly correspond to the theoretical drive reference. The current validation is also limited to a commercial desktop FDM printer configured with PLA and regular toolpaths in the 40–80 mm/s constant-velocity range. The proposed mapping may be sensitive to changes in printer mechanical structure, including stepper motor characteristics, belt tension, frame stiffness, carriage mass, and sensor position, because these factors can affect the prominence and observability of the drive-related dominant component. Flexible materials such as TPU may further alter load transfer and extrusion-related dynamics, while contour paths involving frequent acceleration and deceleration can violate the steady or near-steady assumption adopted here. More broadly, recent studies have shown that material history, thermal evolution, and process–structure–property interactions can also influence printability and mechanical performance in material-extrusion-based additive manufacturing [4,38–40]. These factors were not included in the present EMT-based validation and should be regarded as part of the wider applicability boundary of the proposed mapping.

Future work will extend the validation range and improve the usability of model parameters. In the short term, additional steady segment tests will be carried out under different toolpath directions, repeated builds, and a wider set of commanded constant velocities to improve repeatability assessment and reduce uncertainty in the parameter calibration procedure. In the medium term, the analysis will be extended to more challenging but practically relevant conditions, including velocity transitions, different sensor locations, transmission-related variation, and broader comparisons across operating settings and material conditions. In the long term, the present EMT-based drive-frequency reference may be integrated into a broader monitoring framework that also considers material-dependent process variability and process–structure–property interactions. Printer-specific calibration, improved parameter identification, and more reliable steady segment screening will be used as practical steps to address the universality limits identified in the present work.

Author Contributions: Conceptualization, H.M. and F.G.; Methodology, X.Z., H.M. and F.G.; Validation, X.Z. and Z.L.; Formal analysis, X.Z., H.M., Z.L. and F.G.; Investigation, X.Z. and Z.L.; Resources, B.H.; Data curation, X.Z.; Writing—original draft, X.Z.; Writing—review & editing, X.Z., H.M., B.H., Z.L. and F.G.; Visualization, X.Z.; Supervision, B.H. and F.G.; Project administration, B.H. All authors have read and agreed to the published version of the manuscript.

Funding: This research received no external funding.

Data Availability Statement: The data presented in this study are available on request from the corresponding author.

Conflicts of Interest: The authors declare no conflict of interest.

References

1. He, H.; Zhu, Z.; Zhang, Y.; Zhang, Z.; Famakinwa, T.; Yang, R. Machine Condition Monitoring for Defect Detection in Fused Deposition Modelling Process: A Review. *Int. J. Adv. Manuf. Technol.* **2024**, *132*, 3149–3178. [CrossRef]
2. Tlegenov, Y.; Lu, W.F.; Hong, G.S. A Dynamic Model for Current-Based Nozzle Condition Monitoring in Fused Deposition Modelling. *Prog. Addit. Manuf.* **2019**, *4*, 211–223. [CrossRef]
3. Yeshiwas, T.A.; Tiruneh, A.B.; Sisay, M.A. A Review Article on the Assessment of Additive Manufacturing. *J. Mater. Sci. Mater. Eng.* **2025**, *20*, 85. [CrossRef]
4. Djonyabe Habiba, R.; Malça, C.; Branco, R. Exploring the Potential of Recycled Polymers for 3D Printing Applications: A Review. *Materials* **2024**, *17*, 2915. [CrossRef]
5. Fu, Y.; Downey, A.; Yuan, L.; Pratt, A.; Balogun, Y. In Situ Monitoring for Fused Filament Fabrication Process: A Review. *Addit. Manuf.* **2021**, *38*, 101749. [CrossRef]
6. Oleff, A.; Küster, B.; Stonis, M.; Overmeyer, L. Process Monitoring for Material Extrusion Additive Manufacturing: A State-of-the-Art Review. *Prog. Addit. Manuf.* **2021**, *6*, 705–730. [CrossRef]
7. Hisham, S.; Fenner Khan, S.; Kamarudin, K. Quality Monitoring for Fused Filament Fabrication Product: A Review. *Int. J. Res. Anal. Rev.* **2022**, *9*, 68–74.
8. Khanafer, K.; Cao, J.; Kokash, H. Condition Monitoring in Additive Manufacturing: A Critical Review of Different Approaches. *J. Manuf. Mater. Process.* **2024**, *8*, 95. [CrossRef]
9. Zhang, S.; Sun, Z.; Long, J.; Li, C.; Bai, Y. Dynamic Condition Monitoring for 3D Printers by Using Error Fusion of Multiple Sparse Auto-Encoders. *Comput. Ind.* **2019**, *105*, 164–176. [CrossRef]
10. Yu, B.; Zhang, H.; Tang, J.; Zhao, Z.; Zhng, X.; He, W.; Chen, X. Multi-View Deep Information Fusion Framework for Online Quality Monitoring and Autonomous Correction in Material Extrusion Additive Manufacturing. *Virtual Phys. Prototyp.* **2025**, *20*, e2500672. [CrossRef]
11. Fu, Y.; Downey, A.R.J.; Yuan, L.; Huang, H.T. Real-Time Structural Validation for Material Extrusion Additive Manufacturing. *Addit. Manuf.* **2023**, *65*, 103409. [CrossRef]
12. Badarinath, R.; Prabhu, V. Real-Time Sensing of Output Polymer Flow Temperature and Volumetric Flowrate in Fused Filament Fabrication Process. *Materials* **2022**, *15*, 618. [CrossRef]
13. Moretti, M.; Senin, N. In-Process Monitoring of Part Warpage in Fused Filament Fabrication through the Analysis of the Repulsive Force Acting on the Extruder. *Addit. Manuf.* **2022**, *49*, 102505. [CrossRef]
14. Katsigiannis, M.; Pantelidakis, M.; Mykoniatis, K.; Purdy, G. Current Monitoring for a Fused Filament Fabrication Additive Manufacturing Process Using an Internet of Things System. *Manuf. Lett.* **2023**, *35*, 933–939. [CrossRef]
15. Rooney, S.; Pitz, E.; Pochiraju, K. AutoML-Driven Diagnostics of the Feeder Motor in Fused Filament Fabrication Machines from Direct Current Signals. *J. Intell. Manuf.* **2025**, *36*, 1999–2016. [CrossRef]
16. Yang, Z.; Jin, L.; Yan, Y.; Mei, Y. Filament Breakage Monitoring in Fused Deposition Modeling Using Acoustic Emission Technique. *Sensors* **2018**, *18*, 749. [CrossRef] [PubMed]
17. Lopes, T.G.; Aguiar, P.R.; Monson, P.M.d.C.; D'Addona, D.M.; Conceição Júnior, P.d.O.; de Oliveira Junior, R.G. Machine Condition Monitoring in FDM Based on Electret Microphone, SVM, and Neural Networks. *Int. J. Adv. Manuf. Technol.* **2023**, *129*, 1769–1786. [CrossRef]
18. Wu, H.; Yu, Z.; Wang, Y. Experimental Study of the Process Failure Diagnosis in Additive Manufacturing Based on Acoustic Emission. *Meas. J. Int. Meas. Confed.* **2019**, *136*, 445–453. [CrossRef]
19. Li, F.; Yu, Z.; Yang, Z.; Shen, X. Real-Time Distortion Monitoring during Fused Deposition Modeling via Acoustic Emission. *Struct. Health Monit.* **2020**, *19*, 412–423. [CrossRef]
20. Moretti, M.; Rossi, A.; Senin, N. In-Process Monitoring of Part Geometry in Fused Filament Fabrication Using Computer Vision and Digital Twins. *Addit. Manuf.* **2021**, *37*, 101609. [CrossRef]

21. Ferraris, E.; Zhang, J.; Van Hooreweder, B. Thermography Based In-Process Monitoring of Fused Filament Fabrication of Polymeric Parts. *CIRP Ann.* **2019**, *68*, 213–216. [CrossRef]
22. Bauriedel, N.; Albuquerque, R.Q.; Utz, J.; Geis, N.; Ruckdäschel, H. Monitoring of Fused Filament Fabrication (FFF): An Infrared Imaging and Machine Learning Approach. *J. Polym. Sci.* **2024**, *62*, 5633–5641. [CrossRef]
23. Tartici, I.; Bartolo, P. Exploring Materials Extrusion in 3D Printing: Real-Time Monitoring, and Machine Learning for Predicting Mechanical Properties. *Procedia CIRP* **2024**, *130*, 86–92. [CrossRef]
24. Isiani, A.; Weiss, L.; Bardaweel, H.; Nguyen, H.; Crittenden, K. Fault Detection in 3D Printing: A Study on Sensor Positioning and Vibrational Patterns. *Sensors* **2023**, *23*, 7524. [CrossRef]
25. Jensen, N.J.; Parker, G.G.; Blough, J.R. Base Vibration Effects on Additive Manufactured Part Quality. *Exp. Tech.* **2024**, *48*, 159–170. [CrossRef]
26. Long, S.; Zhao, X.; Shangguan, W.B.; Zhu, W. Modeling and Validation of Dynamic Performances of Timing Belt Driving Systems. *Mech. Syst. Signal Process.* **2020**, *144*, 106910. [CrossRef]
27. Sharma, M.A.; Patterson, A.E. Non-Linear Dynamic Modeling of Cartesian-Frame FFF 3-D Printer Gantry for Predictive Control. In Proceedings of the 34th Annual International Solid Freeform Fabrication (SFF) Symposium—An Additive Manufacturing Conference, Austin, TX, USA, 14–16 August 2023; pp. 686–699. [CrossRef]
28. Olowe, M.; Ogunsanya, M.; Best, B.; Hanif, Y.; Bajaj, S.; Vakkalagadda, V.; Fatoki, O.; Desai, S. Spectral Features Analysis for Print Quality Prediction in Additive Manufacturing: An Acoustics-Based Approach. *Sensors* **2024**, *24*, 4864. [CrossRef] [PubMed]
29. Rais, M.H.; Li, Y.; Ahmed, I. Spatiotemporal G-Code Modeling for Secure FDM-Based 3D Printing. In Proceedings of the ACM/IEEE 12th International Conference on Cyber-Physical Systems, Nashville, TN, USA, 19–21 May 2021; pp. 177–186. [CrossRef]
30. Bednarski, B.; Jackiewicz, K.; Gałecki, A. Influence of Microstepping Signal Shape on Shaft Movement Precision and Torque Variation of the Stepper Motor. *Energies* **2021**, *14*, 6170. [CrossRef]
31. Pillans, J. Reducing Position Errors by Vibration Optimization of Stepper Motor Drive Waveforms. *IEEE Trans. Ind. Electron.* **2021**, *68*, 5176–5183. [CrossRef]
32. Kim, W.; Shin, D.; Lee, Y.; Chung, C.C. Simplified Torque Modulated Microstepping for Position Control of Permanent Magnet Stepper Motors. *Mechatronics* **2016**, *35*, 162–172. [CrossRef]
33. Arias, A.; Caum, J.; Ibarra, E.; Grino, R. Reducing the Cogging Torque Effects in Hybrid Stepper Machines by Means of Resonant Controllers. *IEEE Trans. Ind. Electron.* **2019**, *66*, 2603–2612. [CrossRef]
34. Iqteit, N.A.; Yahya, K.; Makahleh, F.M.; Attar, H.; Amer, A.; Solyman, A.A.A.; Qudaimat, A.; Tamizi, K. Simple Mathematical and Simulink Model of Stepper Motor. *Energies* **2022**, *15*, 6159. [CrossRef]
35. Melmuka, F. A Survey of Models, Analysis Tools and Compensation Methods for the Control of Machines with Friction. *Automatica* **1994**, *30*, 1083–1138. [CrossRef]
36. Liu, Y.F.; Li, J.; Zhang, Z.M.; Hu, X.H.; Zhang, W.J. Experimental Comparison of Five Friction Models on the Same Test-Bed of the Micro Stick-Slip Motion System. *Mech. Sci.* **2015**, *6*, 15–28. [CrossRef]
37. Lopes, T.G.; Aguiar, P.R.; Junior, C.S.; de Oliveira Junior, R.G.; Monson, P.M.C.; David, G.A. Study of the Temperature Influence on an Electret Microphone in the Monitoring of Fused Deposition Modeling. *Eng. Proc.* **2023**, *58*, 64. [CrossRef]
38. Koc Gunessu, H.B.; Atakok, G.; Kam, M. Toward High-Value Circular Pathways for Polymer Waste: Process–Structure–Property Strategies in Mechanical Recycling, Filament Re-Extrusion, and Additive Manufacturing. *Polymers* **2026**, *18*, 607. [CrossRef]
39. Elmoghazy, A.; Heuer, A.; Kneer, A.; Reder, M.; Prahs, A.; Schneider, D.; Liebig, W.V.; Nestler, B. Phase-Field Modeling of the Morphological and Thermal Evolution of Additively Manufactured Polylactic Acid Layers and Their Influence on the Effective Elastic Mechanical Properties. *Prog. Addit. Manuf.* **2025**, *10*, 5093–5115. [CrossRef]
40. Agbakoba, V.C.; Webb, N.; Jegede, E.; Phillips, R.; Hlangothi, S.P.; John, M.J. Mechanical Recycling of Waste PLA Generated from 3D Printing Activities: Filament Production and Thermomechanical Analysis. *Macromol. Mater. Eng.* **2024**, *309*, 2300276. [CrossRef]

Disclaimer/Publisher's Note: The statements, opinions and data contained in all publications are solely those of the individual author(s) and contributor(s) and not of MDPI and/or the editor(s). MDPI and/or the editor(s) disclaim responsibility for any injury to people or property resulting from any ideas, methods, instructions or products referred to in the content.